Ultramicroscopy 109 (2009) 172–176

Contents lists available at ScienceDirect

Ultramicroscopy

journal homepage: www.elsevier.com/locate/ultramic

Column-by-column compositional mapping by *Z*-contrast imaging

S.I. Molina [a,*,1], D.L. Sales [a], P.L. Galindo [b], D. Fuster [c], Y. González [c], B. Alén [c], L. González [c], M. Varela [d], S.J. Pennycook [d]

[a] Departamento de Ciencia de los Materiales e I.M. y Q.I., Facultad de Ciencias, Universidad de Cádiz, Campus Río San Pedro, s/n, 11510 Puerto Real, Cádiz, Spain
[b] Departamento de Lenguajes y Sistemas Informáticos, CASEM, Universidad de Cádiz, Campus Río San Pedro, s/n, 11510 Puerto Real, Cádiz, Spain
[c] Instituto de Microelectrónica de Madrid (CNM, CSIC), Isaac Newton 8, 28760 Tres Cantos, Madrid, Spain
[d] Materials Science and Technology Division, Oak Ridge National Laboratory, Oak Ridge, TN 37831, USA

ARTICLE INFO

Article history:
Received 8 October 2007
Received in revised form
30 June 2008
Accepted 7 October 2008

PACS:
81.70.Jb
61.16.Bg

Keywords:
High-resolution electron microscopy
Z-contrast imaging
Compositional mapping

ABSTRACT

A phenomenological method is developed to determine the composition of materials, with atomic column resolution, by analysis of integrated intensities of aberration-corrected *Z*-contrast scanning transmission electron microscopy images. The method is exemplified for $InAs_xP_{1-x}$ alloys using epitaxial thin films with calibrated compositions as standards. Using this approach we have determined the composition of the two-dimensional wetting layer formed between self-assembled InAs quantum wires on InP(0 0 1) substrates.

© 2008 Elsevier B.V. All rights reserved.

1. Introduction

The development of aberration-corrected scanning transmission electron microscopes has represented an unquestioned breakthrough. Since their implementation [1–4], a huge improvement of the capabilities of these microscopes has taken place, enabling materials to be investigated with sub-Ångstrom resolution [5]. The combination of incoherent *Z*-contrast imaging with spatially resolved electron energy loss spectroscopy (EELS) has provided the possibility of investigating the structure and composition of materials with atomic resolution for more than one decade [6–8]. This combined methodology has experienced an enormous advance in terms of better resolution and enhanced signal-to-noise ratio since the incorporation of aberration correctors into scanning transmission electron microscopes [9–10]. Qualitative high-resolution compositional maps have been obtained from *Z*-contrast images of a number of material systems [11]. However, quantitative compositional maps have only been determined in a few particular cases, such as doped monocrystalline materials [12], structural defects [13], interfaces [14–16] and strained nanostructures [17]. The procedure used mainly to extract quantitative compositional information from high-resolution *Z*-contrast images is based on the comparison of simulated and experimental images. However, experimental *Z*-contrast images show a background signal or an incoherent broadening of the probe [18], which is not predicted by dynamical simulations and complicates the quantitative extraction of compositions directly by image simulation [16].

In this work we introduce a phenomenological method to determine quantitatively the composition of a material with atomic column spatial resolution. The method is based on the analysis of local integrated intensities of aberration-corrected *Z*-contrast images. A set of reference samples of known composition is used to quantify the relationship between the experimental *Z*-contrast intensities and the thickness and composition of the analysed material. The application of this method is exemplified for the $InAs_xP_{1-x}$ alloy. A series of $InAs_xP_{1-x}$ thin films grown on InP(0 0 1) by molecular beam epitaxy (MBE) were used as compositional reference samples. This method is then applied to determine, with atomic column spatial resolution, the composition of a two-dimensional wetting layer formed between low-density self-assembled InAs quantum wires.

2. Experimental section

Three 500 nm thick epitaxial layers were grown at 1 monolayer per second (ML/s) on InP by solid source MBE on InP(0 0 1) substrates at a substrate temperature of 450 °C. The beam

* Corresponding author. Tel.: +34 956 016336; fax: +34 956 016288.
E-mail address: sergio.molina@uca.es (S.I. Molina).
[1] On sabbatical leave at Materials Science and Technology Division, Oak Ridge National Laboratory, Oak Ridge, TN 37831, USA.

0304-3991/$ - see front matter © 2008 Elsevier B.V. All rights reserved.
doi:10.1016/j.ultramic.2008.10.008

equivalent pressure ratios between As_4 and P_2 (As_4/P_2) were varied to form $InAs_xP_{1-x}$ with different compositions: $As_4/P_2 = 0.13$, 0.30 and 0.56. The As compositions obtained for the three epitaxial layers were 0.27, 0.59 and 0.87, respectively. These samples were used as compositional references in this work and we named them S27, S59 and S87. The composition of $InAs_xP_{1-x}$ samples was determined by X-ray diffraction in an X'Pert MRD Philips diffractometer with 4 crystal Ge(2 2 0) as incident beam optic. The (+ −) Bragg arrangement for the (0 0 4) reflection and the (θ+Φ) (θ−Φ) arrangement for (1 1 5) reflections were used. These four diffractograms were taken in both [1 1 0] and [1 $\bar{1}$ 0] directions for each sample. From the recorded data and using a dynamical simulation program we have obtained the alloy composition and the strain state in the $InAs_xP_{1-x}$ samples.

The sample under study (sample W) consists of low-density InAs quantum wires (around 3–4 wires/μm^2) grown on InP(0 0 1). After deposition of a 180 nm thick InP buffer layer the InP surface was exposed to As_4 flux for 3 s at a substrate temperature $T_S = 480\,^\circ$C. InAs was deposited at a deposition rate of 0.5 ML/s, $T_S = 480\,^\circ$C and beam equivalent pressure of $As_4 = 4 \times 10^{-6}$ mbar. After InAs deposition, the surface was annealed for 1.5 min under As_4 flux followed by growth of a 20 nm thick InP cap layer by atomic layer MBE at $T_S = 380\,^\circ$C. In this work, we study the composition of the $InAs_xP_{1-x}$ wetting layer between the quantum wires. More details about the growth and morphology of this kind of sample can be found elsewhere [19].

High-resolution aberration-corrected *Z*-contrast images were taken from both $InAs_xP_{1-x}$ and InP regions of different thickness in the three reference samples. *Z*-contrast images were acquired at 100 kV with a dedicated VG Microscopes HB501UX scanning transmission electron microscope equipped with a Nion aberration-corrector and a Gatan Enfina EELS detector. The 3rd and 5th order spherical aberration coefficients are (nominally) −50 μm and 63 mm, respectively, the inner detector angle is 64 mrad and the objective aperture angle is 27 mrad. Specimens for *Z*-contrast imaging were produced by mechanical thinning and Ar^+ ion milling using a Precision Ion Polishing System (PIPS). Milling conditions were carefully controlled to reproduce as similarly as possible the specimen preparation procedure of the reference samples and sample W, the analysis of which we will show later. The Ar^+ PIPS was used in such a way that the beam always hits the sample from the same direction, which has been found to produce cleaner surfaces in the region of interest. A beam energy less than 3.5 kV has been selected to reduce amorphisation of InP. As a final step, the sample was introduced in a Fischione ion mill at 15° and 0.5 kV to reduce surface damage. The thickness of each analysed region was determined from the analysis of the corresponding spatially resolved low-loss EELS signal, by using the mean free path determined for each *x* composition of the three $InAs_xP_{1-x}$/InP reference samples, according to the method described in Ref. [20].

3. Results and discussion

We have taken a number of high-resolution *Z*-contrast images for each reference sample in regions of different thickness. For each recorded image, corresponding to a particular composition and thickness value, we have analysed the intensity integrated in an area surrounding the group V atomic columns. Herewith we explain, as an example, the analysis carried out in a *Z*-contrast image taken from sample S27 in a region with a thickness of 36 nm. The process exemplified here for sample S27 has been repeated for all the reference compositions (samples S27, S59 and S87) in several regions with different thickness values.

Fig. 1(a) shows an aberration-corrected *Z*-contrast image taken from sample S27 along [1 1 0] in a region with a thickness of 36 nm. The dumbbells are not quite resolved in the *Z*-contrast images, in that not all dumbbells show a 10% dip in intensity, which we use as the criterion for resolution [21], as shown in the inset of Fig. 1(b). However, line traces across the dumbbells do clearly show the two column locations. Pixels with the local intensity maxima associated to In atomic columns are detected on this image by applying the Peak Pairs software [22]. Once these maxima intensity pixels are located, it is straightforward, with the help of image processing software, to measure the intensities integrated within a selected area of the projected unit cell, as shown in Fig. 1(b). Starting with the raw *Z*-contrast image, the resulting integrated intensities from a region of $InAs_{0.27}P_{0.73}$, are shown superposed on the corresponding experimental image in Fig. 1(c). Integrated intensities corresponding to each AsP column are represented in this figure by a coloured circle. The integrated intensity averaged in this way on 517 different group V atomic columns is 17,145 counts. The standard deviation of this measurement is 168 counts, i.e. about 1%. Similarly, this process has been repeated in a nearby region of the InP substrate with the same thickness (36 nm). The average integrated intensity is 16,096 counts for InP, with a standard deviation of 1.3%. The quotient of the average integrated intensity in InP divided by the integrated intensity in $InAs_{0.27}P_{0.73}$ which is 1.0652. We denote this experimental quotient by *R* and we will name it "normalized integrated intensity".

We have repeated the measurement of the normalized integrated intensities *R*, following a procedure similar to the one explained in the previous paragraph for sample S27, for the three reference samples, S27, S59 and S87, for a number of specimen thicknesses values. Table 1 shows the measured *R* values from three thickness values for each reference sample, that is, for each reference composition. The third and fourth columns of this table correspond to the average *R* value in the range of analysed thickness values and the *R* standard deviation, respectively. From the analysis of this table it is clear that the dependence of *R* on the composition is significant but its dependence on the specimen thickness is very small. Fig. 2 represents the average normalized integrated intensities ($R_{average}$) measured for the three reference $InAs_xP_{1-x}$ compositions (27%, 59% and 87%). To simplify, from now on we will write *R* to represent the average normalized integrated intensities. The error bars on this figure correspond to the standard deviation associated with the variation of the *R* values within the selected range of specimen thickness. The maximum standard deviation is 1.5% and corresponds to sample S59.

Now, *R* values could be measured following the same procedure on a heterogeneous $InAs_xP_{1-x}$ alloy, and the composition could be determined, atomic column by atomic column, simply from a linear regression equation that relates *R* with *x* in the standard samples. From the data represented in Fig. 2, our fitting equation becomes

$$R(x) = 1.00462 + 0.229073x. \quad (1)$$

A correlation coefficient of 0.9974 corresponds to this linear fit. These compositional measurements will remain valid over the range of thickness where *R* was found to be almost independent of thickness in the reference samples.

It is worth noting that the area of integration shown in Fig. 1(b) was selected because it has several attractive characteristics: (i) *R* depends almost linearly on the As composition, (ii) *R* has a very low dependence on specimen thickness over a convenient range, (iii) *R* values are almost unaffected by surrounding dumbbells so that the signal is essentially due to the As and P content contained within the selected atomic column. Statements (i) and (ii) are based on our experimental observations. To support statement (iii), we have applied the method to simulated images of one

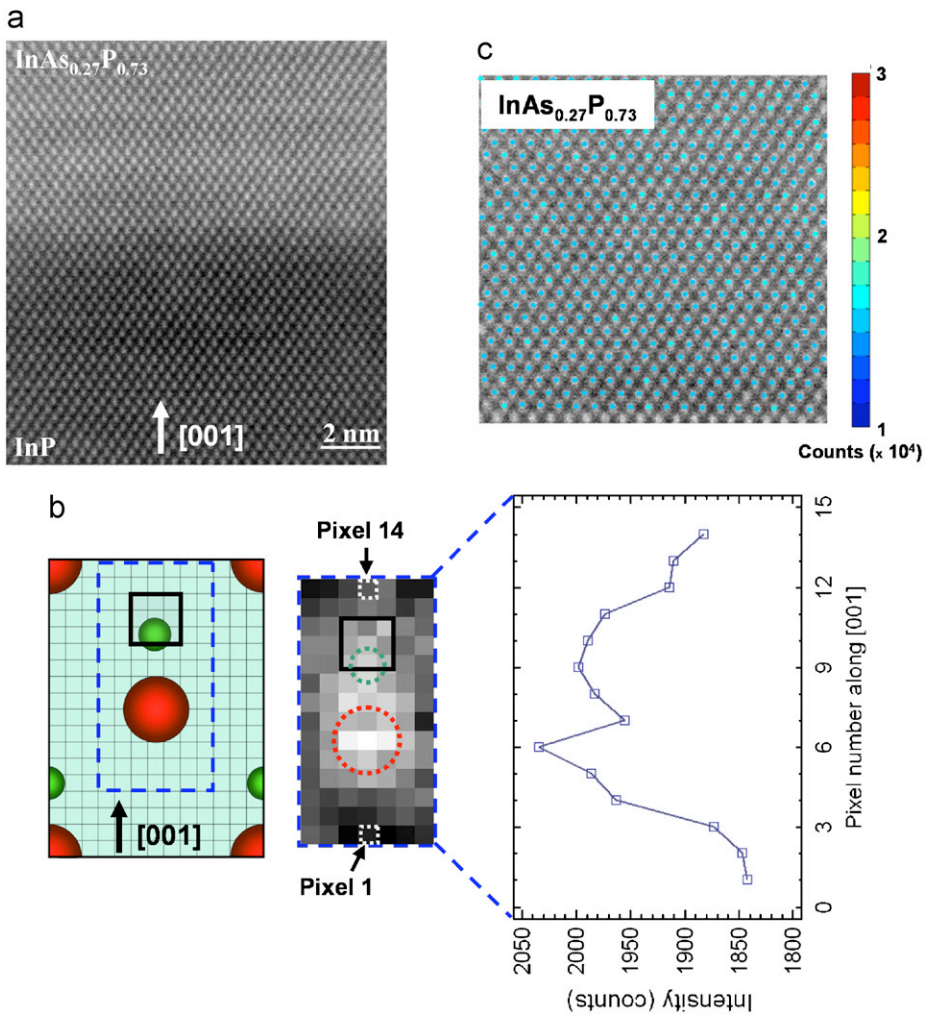

Fig. 1. (a) Raw data high-resolution aberration-corrected *Z*-contrast image taken along [1 1 0] from the interface $InAs_{0.27}P_{0.73}$/InP of sample S27. (b) Area selected (black square of 9 pixels) for each group V column to integrate intensities and calculate *R* ratios, drawn on an experimental raw *Z*-contrast image (right) and the projected unit cell (left). Projected positions of In and group V atomic columns are represented with red and green colour circles. The intensity profile has been taken along [0 0 1] across the central line of the shown image. (c) Integrated intensities in the area selected in (b) superimposed on the high-resolution *Z*-contrast image from which were determined for each analysed group V column. Note that intensity distribution is very homogeneous throughout the whole analysed image.

Table 1
R (measured) values for different specimen thickness (*t*) values, average *R* values ($R_{average}$) and *R* standard deviation (σ_R) for each analysed reference composition.

t (nm)	*R*	$R_{average}$	σ_R
$x = 0.27$			
17.9	1.0736	1.0699	0.0043
24.1	1.0708		
35.8	1.0652		
$x = 0.59$			
16.1	1.1295	1.1468	0.0151
28.5	1.1573		
40.0	1.1537		
$x = 0.87$			
20.0	1.2107	1.1981	0.0118
25.4	1.1963		
30.2	1.1872		

dumbbell of InP embedded in InAs using the approach developed by Ishizuka [23]. The *R* value simulated for the embedded P column is only 4.8% higher than that for pure InP, indicating a false As concentration of ~5%. This represents an extreme example of compositional inhomogeneity, and the most practical cases will be far less severe. The use of larger areas of integration leads to a decrease of the spatial resolution of this method or to more complex dependences of *R* on the thickness and/or the composition. It is worth mentioning that the selection of area marked in Fig. 1(b) has been feasible in our experiments because extreme care was taken during STEM specimen preparation and this has reduced the noise in our images caused by surface amorphous layers. If the contamination or damage of the specimen surface is too large, we have verified that larger areas (or even the entire projected unit cell) have to be used for integration, with a loss in spatial resolution. We think that this is due to the broadening of the electron beam originated by the above-mentioned surface problems, which result in an enhanced delocalization of the scattered electrons collected by the annular dark field detector.

Next, in order to demonstrate the application of this method, we have determined the composition across the $InAs_xP_{1-x}$ wetting layer found between the quantum wires in sample W. Fig. 3(a) shows an aberration-corrected *Z*-contrast image of this wetting layer, which has been acquired using the same imaging and specimen preparation conditions used for the reference samples.

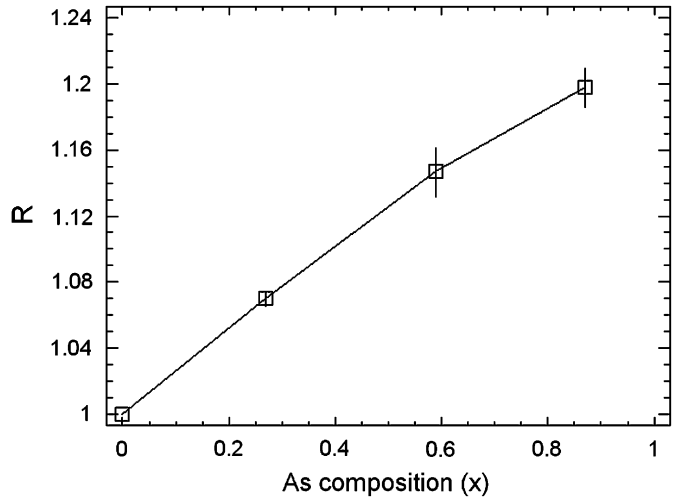

Fig. 2. Experimental R ratios represented versus the As composition of an $InAs_xP_{1-x}$ alloy.

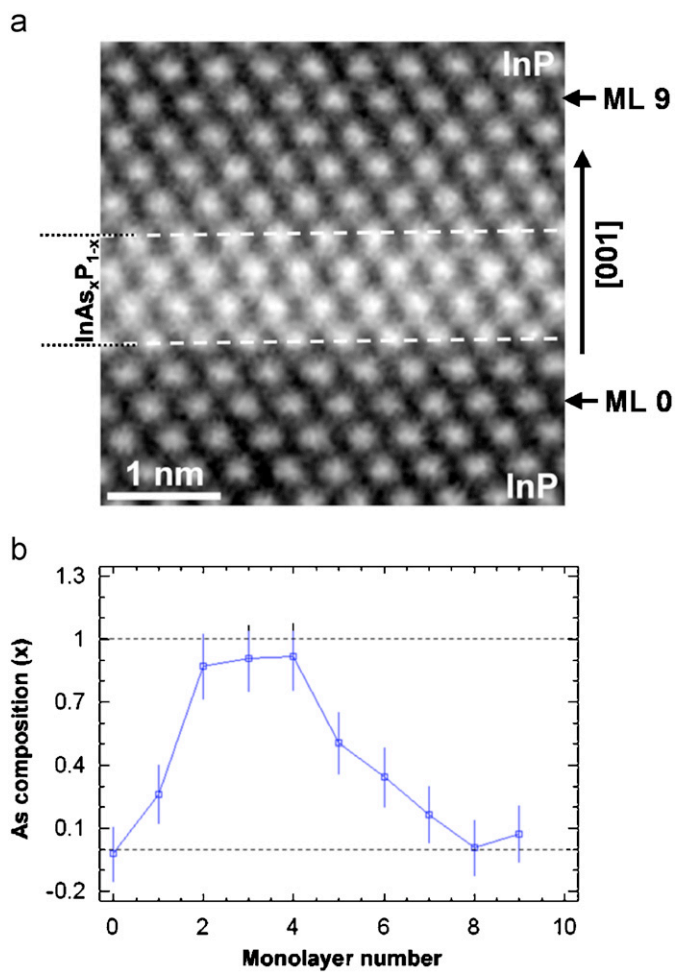

Fig. 3. (a) High-resolution Z-contrast image of the wetting layer of sample W. (b) Compositional profile taken along [0 0 1] across the wetting layer. Monolayers #0 and #9 are marked on the right edge of the image as ML 0 and ML 9, respectively.

The thickness of the electron-transparent specimen measured in this region is 21 ± 1 nm. Fig. 3(b) shows the As compositional profile along [0 0 1] obtained by measuring the $R(x)$ associated with each dumbbell and determining the x values from Eq. (1). The compositional analysis has been carried out for each individual atomic column choosing the regions of the specimen with maximum homogeneity of the integrated intensity in the substrate InP material, i.e. with minimum local specimen thickness changes. The center of the layer shows nearly 100% As concentration and the bottom interface is sharper than the top one. The compositional profile obtained here supports the compositions indirectly determined on the same analysed wetting layer by photoluminescence in previous work [24].

Error bars of the graph of Fig. 3(b) include: (i) errors associated with the assumption that R is independent of the specimen thickness, (ii) the standard deviation of intensities measured in several atomic columns both in InP and the wetting layer and (iii) a contribution from neighbouring columns obtained from simulations, as discussed previously. Errors are quantified as the quadratic mean of all these errors. The background signal is less localized than the intensity ratio R and errors due to this probably represent the greatest unknown in this method at present, and further investigation is needed. This effect will always result in an overestimation of the width of an interface. Hence, in Fig. 3(b), the composition in plane 1 could be less than indicated due to an enhanced background from plane 2. However, such effects will be greatly diminished in planes 5–7, so that the extended As concentration in the tail, and the asymmetric nature of the profile, are certainly real effects.

4. Conclusion

In summary, a method has been developed to determine the composition of materials with atomic column spatial resolution from the analysis of aberration-corrected Z-contrast images. The method has proven to be applicable to a material consisting of a heterogeneous $InAs_xP_{1-x}$ distribution. We propose that use of this procedure, based on the quantification of R values from a series of standard calibrated samples, could be extended as a general method to measure the composition of crystalline materials with atomic column spatial resolution.

Acknowledgements

This work was supported by the Office of Basic Energy Sciences, Division of Materials Sciences and Engineering, US DOE (MV and SJP), the SANDiE European Network of Excellence (Contract No NMP4-CT-2004-500101), the Spanish MEC (TEC2005-05781-C03-01 y 02, NAN2004-09109-C04-01, Consolider-Ingenio 2010 CSD2006-00019), the CAM (S 0505ESP 0200) and the Junta de Andalucia (PAI research groups TEP-120 and TIC-145; project No PAI05-TEP-00383).

References

[1] M. Haider, H. Rose, S. Uhlemann, E. Schwan, B. Kabius, K. Urban, Ultramicroscopy 75 (1998) 53.
[2] M. Haider, S. Uhlemann, E. Schwan, H. Rose, B. Kabius, K. Urban, Nature 392 (1998) 768.
[3] O.L. Krivanek, N. Dellby, A.R. Lupini, Ultramicroscopy 78 (1999) 1.
[4] N. Dellby, O.L. Krivanek, P.D. Nellist, P.E. Batson, A.R. Lupini, J. Electron Microsc. 50 (2001) 177.
[5] P.D. Nellist, M.F. Chisholm, N. Dellby, O.L. Krivanek, M.F. Murfitt, Z.S. Szilagyi, A.R. Lupini, A. Borisevich, W.H. Sides Jr., S.J. Pennycook, Science 305 (2004) 1741.
[6] N.D. Browning, M.F. Chisholm, S.J. Pennycook, Nature 366 (1993) 143.
[7] P.E. Batson, Nature 366 (1993) 727.
[8] N.D. Browning, S.J. Pennycook, J. Phys. D 29 (1996) 1779.
[9] S.J. Pennycook, M. Varela, C.J.D. Hetherington, A.I. Kirkland, Mater. Res. Bull. 31 (2006) 36.

[10] M. Varela, A.R. Lupini, K. van Benthem, A.Y. Borisevich, M.F. Chisholm, N. Shibata, E. Abe, S.J. Pennycook, Ann. Rev. Mater. Res. 35 (2005) 539.
[11] E. Carlino, S. Modesti, D. Furlanetto, M. Piccin, S. Rubini, A. Franciosi, Appl. Phys. Lett. 83 (2003) 662.
[12] P.M. Voyles, D.A. Muller, J.L. Grazul, P.H. Citrin, H.-J.L. Gossmann, Nature 416 (2002) 826.
[13] T. Yamazaki, N. Nakanishi, A. Recnik, M. Kawasaki, K. Watanabe, M. Ceh, M. Shiojiri, Ultramicroscopy 98 (2004) 305.
[14] S.C. Anderson, C.R. Birkeland, G.R. Anstis, D.J.H. Cockayne, Ultramicroscopy 69 (1997) 83.
[15] R.F. Klie, Y. Zhu, Micron 36 (2005) 219.
[16] D.O. Klenov, S. Stemmer, Ultramicroscopy 106 (2006) 889.
[17] P. Wang, A.L. Bleloch, M. Falke, P.J. Goodhew, J. Ng, M. Missous, Appl. Phys. Lett. 89 (2006) 072111.
[18] J.M. LeBeau, S.D. Findlay, L.J. Allen, S. Stemmer, Phys. Rev. Lett. 100 (2008) 206101.
[19] D. Fuster, B. Alén, L. González, Y. González, J. Martínez-Pastor, M.U. González, J.M. García, Nanotechnology 18 (2007) 035604.
[20] R.F. Egerton, Electron Energy-Loss Spectroscopy in the Electron Microscope, Plenum Press, New York, 1986.
[21] Y. Peng, M.P. Oxley, A.R. Lupini, M.F. Chisholm, S.J. Pennycook, Microsc. Microanal. 14 (2008) 36.
[22] P.L. Galindo, S. Kret, A.M. Sanchez, J.-Y. Laval, A. Yañez, J. Pizarro, E. Guerrero, T. Ben, S.I. Molina, Ultramicroscopy 107 (2007) 1186.
[23] K.A. Izhizuka, Ultramicroscopy 90 (2002) 71.
[24] B. Alén, D. Fuster, Y. González, L. González, J. Martínez-Pastor, Appl. Phys. Lett. 89 (2006) 233126.